

A near-global climatology of oceanic coherent eddies

Josué Martínez-Moreno¹, Andrew McC. Hogg¹, and Matthew H. England²

¹Research School of Earth Science and ARC Center of Excellence for Climate Extremes, Australian National University, Canberra, Australia

²Climate Change Research Centre (CCRC), UNSW Australia, Sydney NSW, Australia

Key Points:

- Coherent eddies contain around 50% of the surface ocean kinetic energy budget.
- Seasonal cycle of the number of coherent eddies and coherent eddy amplitude reveal a 3-6 month lag to wind forcing.
- The seasonal lag between the number and the amplitude of coherent eddies suggests a role for the inverse cascade.

Corresponding author: Josué Martínez-Moreno, josue.martinezmoreno@anu.edu.au

12 Abstract

13 Ocean eddies influence regional and global climate through mixing and transport of heat
14 and properties. One of the most recognizable and ubiquitous feature of oceanic eddies
15 are coherent vortices with spatial scales of tens to hundreds of kilometers, frequently re-
16 ferred as “mesoscale eddies”. Coherent mesoscale eddies are known to transport prop-
17 erties across the ocean and to locally affect near-surface wind, cloud properties and rain-
18 fall patterns. Although coherent eddies are ubiquitous, their climatology, seasonality and
19 long-term temporal evolution remains poorly understood. Here, we examine the kinetic
20 energy contained by coherent eddies and present the seasonal, inter-annual and long-term
21 variability of ~ 37 million coherent eddies features detected from satellite observations
22 between 1993 to 2019. Around 50% of the kinetic energy contained by ocean eddies cor-
23 responds to coherent eddies. Additionally, a strong seasonal cycle is observed, with a 3–
24 6 months lag between the wind forcing and the response of the coherent eddy field. The
25 seasonality of the number of coherent eddies and their amplitude reveals that the num-
26 ber of coherent eddies responds faster to the forcing (~ 3 months), than the coherent eddy
27 amplitude (which is lagged by ~ 6 months). This seasonal cycle of the coherent eddy prop-
28 erties is spatially variable, thus we also analyze the coherent eddy climatology in key oceanic
29 regions. Our analysis highlights the relative importance of the coherent eddy field in the
30 ocean kinetic energy budget, implies a strong response of the eddy number and eddy am-
31 plitude to forcing at different time-scales, and showcases the seasonality, and multidecadal
32 trends of coherent eddy properties.

33 Plain language summary

34 Coherent eddies are the most common feature of ocean variability observable from
35 satellites. They are crucial in ocean dynamics as they can transport properties over long
36 distances and interact with the atmosphere. Our study investigates the seasonal, inter-
37 annual, and long-term changes in the abundance and intensity of coherent eddies, by au-
38 tomatically identifying individual eddies over the available satellite altimeter record. The
39 seasonal cycle suggests a transition from numerous, smaller, and weaker coherent eddies,
40 to fewer and larger, and stronger coherent eddies over the season. In addition, a long-
41 term adjustment of the coherent eddy field is identified with possible links to long-term
42 changes in the climate system.

43 **1 Introduction**

44 Mesoscale ocean variability with spatial scales of tens to hundreds of kilometers is
 45 comprised of processes such as vortices, waves, and jets (Ferrari & Wunsch, 2009; Fu et
 46 al., 2010). These mesoscale processes are highly energetic, and they play a crucial role
 47 in the transport of heat, salt, momentum, and other tracers through the ocean (Wun-
 48 sch & Ferrari, 2004; Wyrtki et al., 1976; Gill et al., 1974). One of the most recognizable
 49 and abundant ocean processes observable from space are mesoscale vortices. Although
 50 mesoscale vortices are commonly referred to in the literature as “mesoscale eddies”, this
 51 term is also often used to describe the total mesoscale ocean variability (the time-varying
 52 component of the mesoscale flow), thus, to avoid ambiguity we will refer to mesoscale
 53 vortices as *coherent eddies*. Coherent eddies are abundant and energetic; therefore they
 54 are also essential to ocean dynamics as concluded by many previous studies (Hogg & Blun-
 55 dell, 2006; Siegel et al., 2011; Beron-Vera et al., 2013; Frenger et al., 2013, 2015; Pilo et
 56 al., 2015; Schubert et al., 2019; Patel et al., 2020).

57 Coherent eddies are quasi-circular geostrophic currents. According to their rota-
 58 tional direction and the sign of the Coriolis parameter, the sea surface height anomaly
 59 within a coherent eddy can have a negative or positive sea surface height anomaly (cold-
 60 core and warm-core coherent eddies, respectively). This characteristic sea surface height
 61 signature of coherent eddies has been utilized to identify and track coherent eddies from
 62 satellite altimetry (e.g., Chelton et al., 2007; Faghmous et al., 2015; Ashkezari et al., 2016;
 63 Martínez-Moreno et al., 2019; Cui et al., 2020). Automated identification algorithms of
 64 coherent eddies have revealed their ubiquity in the oceans, with a predominant influence
 65 at hotspots of eddy activity such as in boundary current extensions and the Antarctic
 66 Circumpolar Current. In these regions, it has been estimated that coherent eddies con-
 67 tribute around 40–50% of the net mesoscale kinetic energy (Chelton et al., 2011) and thus
 68 a significant fraction of the total kinetic energy (Ferrari & Wunsch, 2009). Although this
 69 estimate showcases the importance of the mesoscale coherent eddy field, the energy con-
 70 tained by coherent eddies was estimated by extracting the total geostrophic velocity within
 71 the radius of each detected coherent eddy; thus, it is possible that this estimate may con-
 72 tain energy from other processes. Here we extend on this past work by reconstructing
 73 the surface imprint of coherent eddies using a new eddy tracking algorithm and using
 74 the latest available satellite record.

75 There is broad consensus that mesoscale eddy kinetic energy has a pronounced sea-
76 sonal variability (Qiu, 1999; Qiu & Chen, 2004; Kang & Curchitser, 2017; Uchida et al.,
77 2017). Several hypotheses have been proposed to explain this seasonality including: sea-
78 sonal variations of atmospheric forcing (Sasaki et al., 2014), seasonality of the mixed layer
79 depth (Qiu et al., 2014; Callies et al., 2015), seasonality of the intensity of barotropic in-
80 stability (Qiu & Chen, 2004), the variability of the baroclinic instability due to the sea-
81 sonality of the vertical shear (Qiu, 1999), and a seasonal lag of the inverse energy cas-
82 cade (i.e. energy is transported between scales, from small to large; Arbic et al., 2013)
83 in combination with the presence of a front in the mixed layer, which can lead to a sea-
84 sonal cycle of the baroclinic instability (Qiu et al., 2014). On one hand, processes such
85 as barotropic and baroclinic instabilities control the seasonality of coherent eddies in the
86 ocean. On the other hand, recent studies using observations and eddy-permitting climate
87 models suggest several long-term adjustments of the global ocean capable of long-term
88 changes in the coherent eddy field. Such readjustments include a multidecadal increase
89 in the ocean stratification resulting from temperature and salinity changes (Li et al., 2020),
90 a horizontal readjustment of sea surface temperature gradients (Cane et al., 1997; Bouali
91 et al., 2017; Ruela et al., 2020), and an intensification of the kinetic energy, eddy kinetic
92 energy, and mesoscale eddy kinetic energy over the last 3 decades as a consequence of
93 an increase in wind forcing (Hu et al., 2020; Wunsch, 2020; Martínez-Moreno et al., 2021).
94 All these seasonal factors and long-term readjustments directly influence the annual and
95 decadal response of the coherent eddy field, however, the seasonality of the coherent com-
96 ponent of the eddy kinetic energy, as well as the seasonal cycle and trends of the coher-
97 ent eddy statistics, remain unknown.

98 Here we present a new global climatology of the coherent eddy kinetic energy by
99 reconstructing the coherent eddy signature from satellite observations. Our study doc-
100 uments the seasonal cycle of the coherent eddy kinetic energy, and the seasonal cycle and
101 long-term trends of the coherent eddy properties over the satellite record. Moreover, we
102 conduct more detailed analyses in regions where coherent eddies dominate the eddy ki-
103 netic energy field. The rest of this paper is structured as follows: the data sources and
104 methodology are described in Section 2. Then, we present the climatology, energy ra-
105 tios, and global seasonality of the coherent eddy kinetic energy in Section 3. Section 4
106 outlines the global climatology and seasonality of coherent eddy properties, followed by
107 long-term changes of the coherent eddy properties (Section 5). Then we focus our at-

108 tention on the seasonal cycle and coherent eddy properties in regions dominated by co-
 109 herent eddies (Section 6). Finally, Section 7 summarizes the main results and discusses
 110 the implications of this study.

111 **2 Methods**

112 We use daily sea surface height (SSH) data made available by the Copernicus Ma-
 113 rine Environment Monitoring Service in near real time (CMEMS, 2017). This gridded
 114 product contains the sea surface height and geostrophic velocities with daily 0.25° res-
 115 olution from January 1993 to 2019. The daily geostrophic velocities allow us to compute
 116 the kinetic energy (KE) and eddy kinetic energy (EKE) over the satellite record. The
 117 main source of EKE is the time-varying wind (Ferrari & Wunsch, 2009); thus, we also
 118 compute the seasonal cycle of the wind magnitude from the JRA55 reanalysis (Japan
 119 Meteorological Agency, Japan, 2013) using wind velocities at 10m above the ocean's sur-
 120 face.

121 Over the same record, coherent eddy statistics from Martínez-Moreno et al. (2019),
 122 hereafter MM19, are analyzed and compared with those released by Chelton & Schlax
 123 (2013), hereafter CS13. Both datasets are gridded in a 1° resolution and are produced
 124 via automated eddy identification algorithms using closed contours of SSH. However, these
 125 datasets have important differences in the criteria they use to identify and record coher-
 126 ent eddies statistics. The major differences include: (i) MM19's algorithm requires an
 127 adjustment between a 2D Gaussian and the SSH anomaly (SSHa) surface within the iden-
 128 tified closed contour, while CS13's only uses the outermost closed contour of SSH; (ii)
 129 MM19's dataset reports the maximum SSHa within the identified coherent eddy, while
 130 CS13's algorithm reports the maximum SSH value minus the discrete level in which the
 131 coherent eddy was identified; and (iii) MM19's dataset includes all detected coherent ed-
 132 dies, while CS13's dataset excludes coherent eddies with lifetimes shorter than four weeks
 133 and coherent eddy amplitudes smaller than 1cm. Moreover, MM19's algorithm allows
 134 the reconstruction of the coherent eddy field under the assumption that coherent eddies
 135 have a 2D Gaussian imprint in the sea surface height. This Gaussian reconstruction of
 136 the coherent eddy field then allows us to estimate the coherent geostrophic eddy veloc-
 137 ities and thus the kinetic energy contained only by coherent eddies.

138 **2.1 Kinetic Energy decomposition**

139 Kinetic energy is commonly divided into the mean and time-varying components
 140 through a Reynolds decomposition. At a given time, the surface velocity field $\mathbf{u} = (u, v)$
 141 is split into the time mean ($\bar{\mathbf{u}}$) and time varying components (\mathbf{u}'). Moreover, MM19 pro-
 142 posed to further decompose the eddy kinetic energy into the energy contained by coher-
 143 ent features (\mathbf{u}'_e) and non-coherent features (\mathbf{u}'_n). Therefore the KE equation can be writ-
 144 ten as:

$$\text{KE} = \underbrace{\bar{u}^2 + \bar{v}^2}_{\text{MKE}} + \underbrace{u'^2_e + v'^2_e}_{\text{CEKE}} + \underbrace{u'^2_n + v'^2_n}_{\text{nCEKE}} + \mathcal{O}_c^2 + \mathcal{O}^2 \quad (1)$$

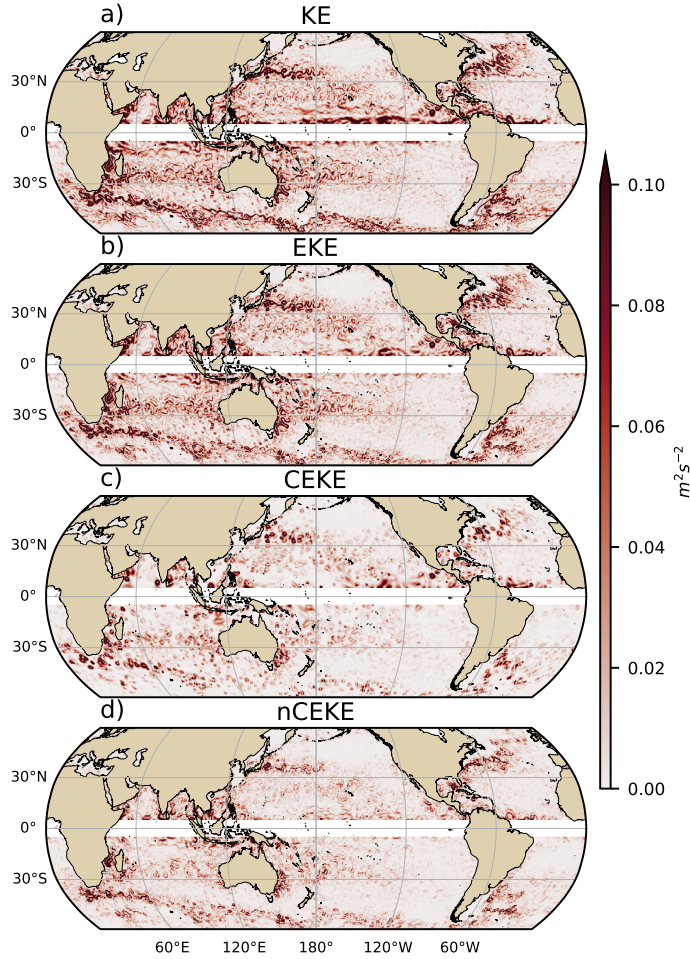
EKE

145 Due to the properties of this decomposition, the second order term \mathcal{O}^2 is zero when
 146 averaged over the same period as $\bar{\mathbf{u}}$. However, \mathcal{O}_c^2 is not necessarily negligible, unless it
 147 is averaged over time and space. More information about the decomposition of the field
 148 into coherent features and non-coherent features is explained in Martínez-Moreno et al.
 149 (2019). A global snapshot of each component of kinetic energy decomposition is shown
 150 in Figure 1, where the KE and EKE are comprised of rings and filaments. As expected,
 151 the decomposition of EKE into CEKE and nCEKE components exhibits only ring-like
 152 signatures expected of coherent eddies, while the non-coherent component shows primar-
 153 ily filaments, with some mis-identified coherent eddies.

157 **2.2 Eddy statistics**

158 The eddy statistics used in this study include (i) the eddy count ($c\text{Eddy}_n$) defined
 159 as the number of coherent eddies per grid cell, (ii) the eddy diameter defined as the di-
 160 ameter of a circle with equal area to the closed contour of each identified eddy, and (iii)
 161 the mean eddy amplitude defined as the mean amplitude of the coherent eddies within
 162 the cell ($c\text{Eddy}_{amp}$). The latter metric can be separated into positive ($c\text{Eddy}_{amp}^+$) and
 163 negative ($c\text{Eddy}_{amp}^-$) coherent eddy amplitudes, defined as the mean amplitude of warm
 164 core and cold core coherent eddies, respectively, within the cell. The polarity indepen-
 165 dent eddy amplitude ($|c\text{Eddy}_{amp}|$) is defined as:

$$|c\text{Eddy}_{amp}| = \frac{1}{2} (c\text{Eddy}_{amp}^+ - c\text{Eddy}_{amp}^-) \quad (2)$$



154 **Figure 1.** Snapshot of surface kinetic energy (\overline{KE}), surface eddy kinetic energy (\overline{EKE}),
 155 surface coherent eddy kinetic energy (\overline{CEKE}), and surface non-coherent eddy kinetic energy
 156 (\overline{nCEKE}) for the 1st of January 2017.

166 Note that the $cEddy_{amp}^+$ and $cEddy_{amp}^-$ are sign definite, thus the difference will always
 167 be positive, whereas the gridded averaged $cEddy_{amp}$ can be negative or positive noting
 168 the dominant polarity of coherent eddies in the region, and the absolute value of $cEddy_{amp}$
 169 is denoted by $cEddy_{|amp|}$. We analyze the climatology and trends of the above eddy statis-
 170 tics over the available satellite record, namely between 1993 and 2019. We exclude the
 171 equatorial region ($10^\circ S - 10^\circ N$) and regions poleward of 60° , because the geostrophic ap-
 172 proximation is invalid near the equator and the satellite spatial coverage at high-latitudes
 173 is unable to resolve the coherent eddy scales polewards of 60° . Note that the climatol-
 174 ogy of $cEddy_n$ is computed by adding all the identified eddies over the record, while all

other climatological statistics are computed as the time-average over the record. Seasonal climatologies are calculated for the monthly average of each coherent eddy statistic, while hemispherical time-series are filtered with a running average of 90 days. Trends of $cEddy_n$ and $|cEddy_{amp}|$ are calculated by coarsening the dataset to a 5° grid, and then linear trends are computed for each grid point. The statistical significance of trends is assessed by a modified Mann-Kendall test above 95% confidence level (Yue & Wang, 2004).

Time averages are denoted by $\overline{}$, while area-weighted averages are denoted using $\langle \rangle$, where the area-weighted average of a function f is:

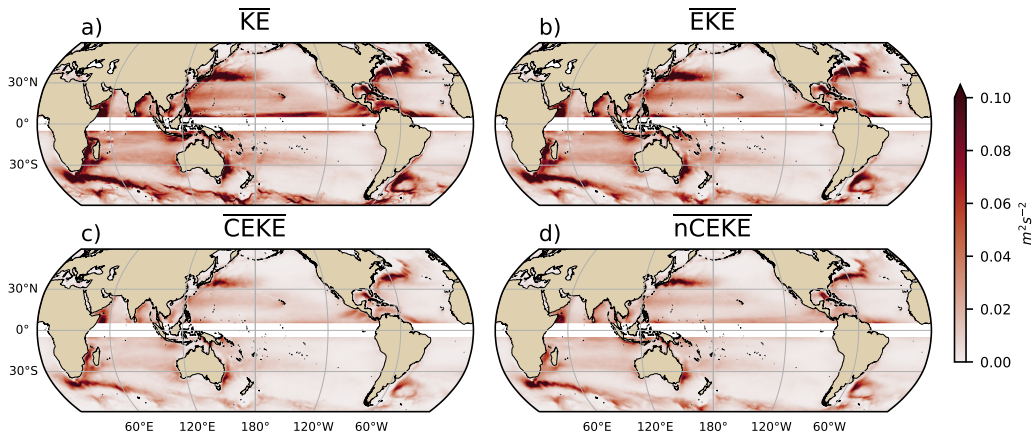
$$\langle f \rangle = \frac{\int f \xi dx dy}{\int \xi dx dy}, \quad (3)$$

where ξ is a mask that is set to zero in grid cells where no coherent eddies were identified.

3 Global Coherent Eddy Energetics

The kinetic energy decomposition estimated from sea surface height measured by satellite altimeters averaged from 1993-2019 is shown in Figure 2. These maps show that many regions of the global ocean are highly energetic in mean KE (\overline{KE}), mean EKE (\overline{EKE}), mean coherent eddy kinetic energy (\overline{CEKE}) and mean non-coherent eddy kinetic energy (\overline{nCEKE}). The spatial pattern highlights well-known regions of the ocean where mesoscale processes are abundant, such as the western boundary current extensions (WBCe) and the Antarctic Circumpolar Current. The spatial distribution of the energy contained by the reconstructed mesoscale coherent eddies and non-coherent components are similar (Figures 2c,d). However, there are some regions where coherent eddies dominate over non-coherent, and vice-versa. Overall, this decomposition suggests that boundary current extensions and other energetic regions of the ocean, particularly eddy-rich regions, contain both coherent and non-coherent components of the kinetic energy.

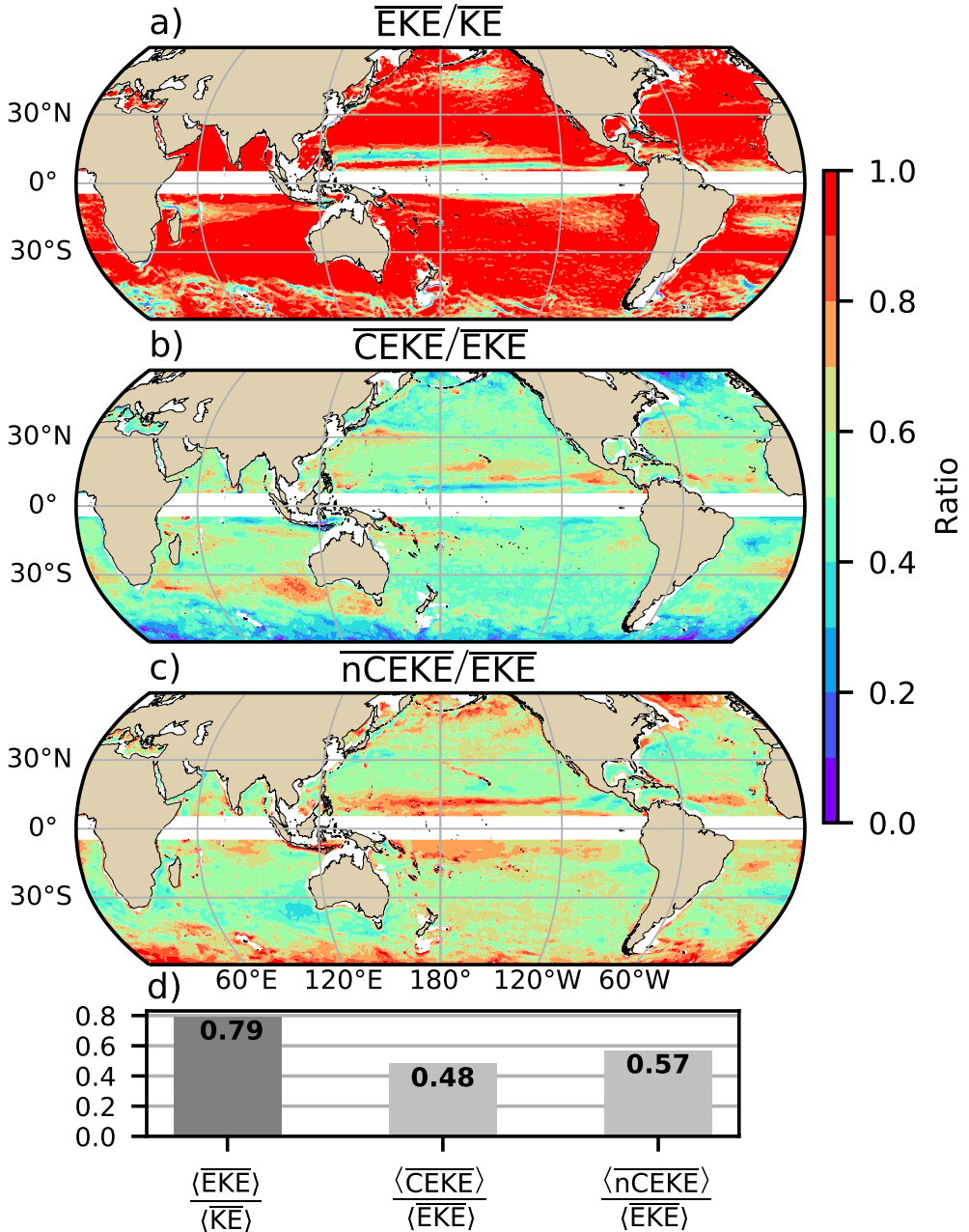
Eddy kinetic energy is known to be more than an order of magnitude greater than kinetic energy of the mean flow (MKE; Gill et al., 1974); this result is clearly shown in Figure 3a, which indicates that \overline{EKE} is responsible for almost all the \overline{KE} across the ocean, except for regions with persistent currents over time. Such regions are located in the mean boundary extension locations, the equatorial Pacific currents and regions in the Antarctic Circumpolar Current, where the \overline{EKE} explains around 40% of the \overline{KE} . In a previous study, Chelton et al. (2011) estimated that the EKE within coherent eddies with life-



198 **Figure 2.** Mean surface kinetic energy (\overline{KE}), surface eddy kinetic energy (\overline{EKE}), surface
199 coherent eddy kinetic energy (\overline{CEKE}), and surface non-coherent eddy kinetic energy (\overline{nCEKE})
200 averaged between 1993-2018.

217 times greater than 4 weeks contain between 40-60% of the \overline{EKE} . Our method to recon-
218 struct the coherent eddy signature (Figure 3b) further corroborates that the coherent
219 eddy component ($\langle \overline{CEKE} \rangle$) has $\sim 48\%$ of the $\langle \overline{KE} \rangle$ (Figure 3d). Furthermore, global area
220 averages of the ratios show that $\langle \overline{EKE} \rangle$ explains $\sim 78\%$ of the ocean $\langle \overline{KE} \rangle$ field, while
221 non coherent eddy features contain $\sim 57\%$ percent of the $\langle \overline{EKE} \rangle$. Note that the globally
222 averaged coherent and non coherent components do not add to 100% as the cross terms
223 (\mathcal{O}_c^2) are non-zero and coherent eddy reconstruction errors. The spatial pattern reveals
224 a dominance of the \overline{CEKE} equatorward from the boundary current extensions and in ar-
225 eas with large coherent eddy contributions of around 80% of the region's eddy kinetic
226 energy, such as south of Australia, in the Tehuantepec Gulf, and in the tropical Atlantic.
227 An evident signal is a reduction of the energy contained by coherent eddies at high lat-
228 itudes and an increase in the energy explained by non-coherent eddies; this signal could
229 be a consequence of the inability of the 0.25° satellite resolution (~ 13 km at 60° lat-
230 itude) to resolve coherent eddies with scales smaller than ~ 10 km (first baroclinic Rossby
231 radius at 60° ; Chelton et al., 1998).

232 Figure 4 shows the seasonal cycle of the area weighted EKE and CEKE for the North-
233 ern Hemisphere ($\langle EKE \rangle_{NH}$ and $\langle CEKE \rangle_{NH}$; $10^\circ N - 60^\circ N$) and Southern Hemisphere
234 ($\langle EKE \rangle_{SH}$ and $\langle CEKE \rangle_{SH}$; $60^\circ S - 10^\circ S$). In both hemispheres, the $\langle EKE \rangle$ and $\langle CEKE \rangle$
235 peak during summer. In the Northern Hemisphere, the largest $\langle EKE \rangle_{NH}$ and $\langle CEKE \rangle_{NH}$



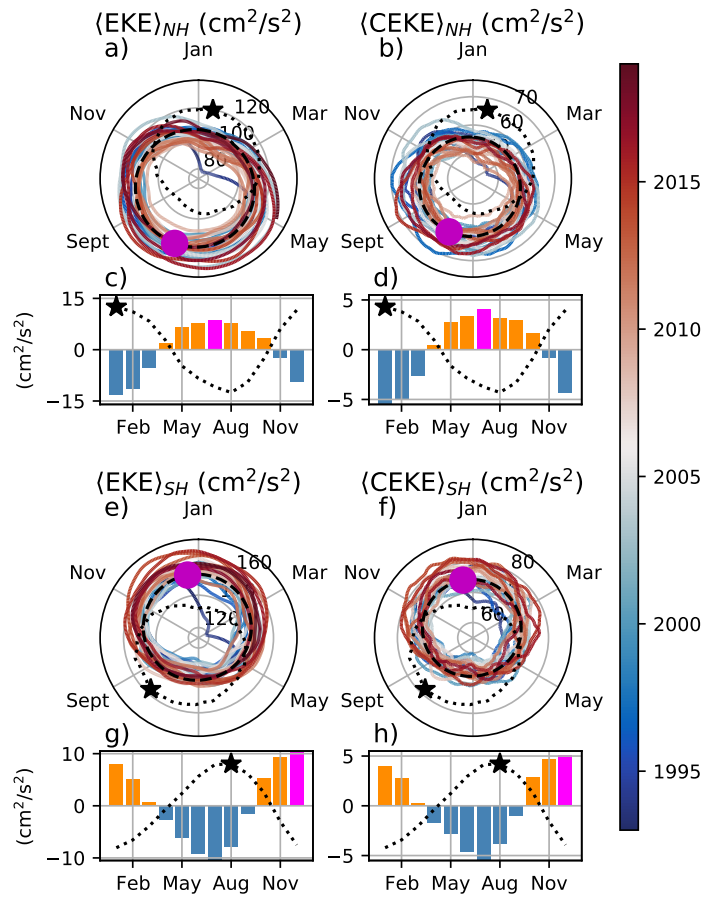
201 **Figure 3.** Ratios of the kinetic energy components. a) Map of the proportion of mean eddy
 202 kinetic energy (\overline{EKE}) versus mean kinetic energy (\overline{KE}); b) Map of the percentage of mean co-
 203 herent eddy kinetic energy (\overline{CEKE}) versus mean eddy kinetic energy (\overline{EKE}); c) Map of the
 204 percentage of mean non-coherent eddy kinetic energy (\overline{nCEKE}) versus mean eddy kinetic energy
 205 (\overline{EKE}); d) Global time and area averaged (represented by $\langle \rangle$) percentage of mean eddy kinetic
 206 energy ($\langle \overline{EKE} \rangle$) versus the global mean kinetic energy ($\langle \overline{KE} \rangle$), area averaged percentage of mean
 207 coherent eddy kinetic energy ($\langle \overline{CEKE} \rangle$) and mean non coherent eddy kinetic energy ($\langle \overline{nCEKE} \rangle$)
 208 versus global mean eddy kinetic energy ($\langle \overline{EKE} \rangle$). Regions where the depth of the ocean is shall-
 209 lower than 1000m are removed from the ratio estimation.

236 occurs in July, \sim 6 months after the maximum winds in January (purple bar and back
 237 star in Figure 4c and d). Meanwhile, the Southern Ocean $\langle \text{EKE} \rangle_{SH}$ and $\langle \text{CEKE} \rangle_{SH}$ sea-
 238 sonal maxima arises during December, \sim 4 months after the maximum winds in August
 239 (purple bar and back star in Figure 4g, and h). This lag between winds and the eddy
 240 and coherent eddy energy components is further discussed in Section 4.

241 The cyclic plots in Figure 4 show the temporal evolution of $\langle \text{EKE} \rangle$ and $\langle \text{CEKE} \rangle$.
 242 Note that high frequency variability can be observed in the $\langle \text{CEKE} \rangle$ field with tempo-
 243 ral scales of a few months, this variability could be attributed to regional dynamics av-
 244 eraged over the hemisphere (boundary currents, ocean gyres, etc.), as well as errors within
 245 the coherent eddy reconstruction. Additionally, concentric changes in the cyclic plots high-
 246 light long-term changes over the record. For example, the Northern Hemisphere winters
 247 during early years of the record (blue) had a more energetic coherent eddy field, which
 248 has transitioned to weaker coherent energy content since 2010 (red), in other words, the
 249 intensity of the $\langle \text{CEKE} \rangle_{NH}$ field has decreased. A larger long-term change can be ob-
 250 served in the Southern Hemisphere, where concentric growth over time in $\langle \text{EKE} \rangle_{SH}$ and
 251 $\langle \text{CEKE} \rangle_{SH}$ support the previously observed strengthening of the eddy field in the South-
 252 ern Ocean (Hogg et al., 2015; Martínez-Moreno et al., 2019; Martínez-Moreno et al., 2021).

262 4 Global Coherent Eddy Statistics

263 Coherent eddy kinetic energy allows us to quantify and study the energy of the eddy
 264 field, but the coherent eddy properties computed by automated coherent eddy identi-
 265 fication algorithms allow us to further investigate in more detail the contribution and
 266 temporal changes of their abundance (i.e. the number of eddies) and their intensity (both
 267 their amplitude and diameter). Figure 5 shows gridded climatologies of the number of
 268 eddies and the eddy amplitude. In this analysis, we contrast our MM19 eddy count with
 269 that of CS13 (Chelton et al., 2007; Figure 5a-b). Although the number of identified ed-
 270 dies is larger in MM19, possibly due to the lifespan filter implemented by CS13, both
 271 datasets reveal consistent spatial patterns. For example, both datasets show an impor-
 272 tant zonal variation in the abundance of eddies, with high numbers of eddies in mid-latitudes
 273 and fewer eddies in the tropics and at high-latitudes ($\sim 60^\circ$). Additionally, there is a ten-
 274 dency at mid-latitudes (30°) of higher number of eddies in the eastern side of ocean basins
 275 (e.g. East North Pacific, East North Atlantic, East South Pacific, and East South At-
 276 lantic). Another interesting pattern emerges in both eddy count datasets, where small



253 **Figure 4.** Seasonality of the area-weighted eddy kinetic energy ($\langle EKE \rangle$) and coherent eddy ki-
 254 netic energy ($\langle CEKE \rangle$). Panels a) and b) show the time-series of the Northern Hemisphere, while
 255 panels e) and f) correspond to the Southern Hemisphere. Panels c) and d) show the seasonal
 256 cycle of the $\langle EKE \rangle_{NH}$ and $\langle CEKE \rangle_{NH}$ in the Northern Hemisphere, and panels g) and h) show
 257 the Southern Hemisphere ($\langle EKE \rangle_{SH}$ and $\langle CEKE \rangle_{SH}$). Dashed lines correspond to the seasonal
 258 cycle of the fields and dotted lines show the seasonal cycle of the wind magnitude smoothed over
 259 120 days (moving average). The black and magenta markers (circle and bar) show the maximum
 260 of the seasonal cycle for the kinetic energy components and the wind magnitude, respectively. In
 261 the cyclic plots, line colors shows the year.

scale structures appear in the eddy count field. These small structures highlight preferred coherent eddy paths observable in boundary current extensions and over regions of the Southern Ocean. These structures and paths of coherent eddies could be associated with topographic features, with overall consistency between the eddy count patterns using the two different eddy identification methods.

Regions with large counts of eddies have in general small absolute amplitudes (Figure 5 c). The ocean gyre interiors have a larger absolute amplitude and finally regions such as the boundary current extensions and the Antarctic Circumpolar Current have the largest coherent eddy absolute amplitudes, as shown also by Chelton et al. (2011). Eddy amplitude highlights regions dominated by a given coherent eddy polarity, for example, boundary extensions have a preferred sign (Figure 5 d); namely, positive amplitude polewards of the boundary current extension mean location, and negative amplitude equatorwards. This sign preference is consistent with the preferential way that coherent eddies are shed from boundary current extensions; with warm core eddies (positive) polewards of the boundary current extension, and equatorward for cold core eddies (negative) (Chelton et al., 2007, 2011; Kang & Curchitser, 2013). These global statistics reveal the absolute coherent eddy amplitude as a proxy for the CEKE with similar spatial patterns (Figure 2 & Figure 5c) and showcases that regions where $\overline{\text{CEKE}}$ has a large proportion of $\overline{\text{EKE}}$ (Figure 3), the absolute coherent eddy amplitude is also large.

To further understand the seasonal cycle of $\langle \text{CEKE} \rangle$, we compute the climatology of coherent eddy properties in each hemisphere (Figure 6). The seasonality of the number of eddies in the Northern Hemisphere peaks in April (Figure 6a, c), while the Southern Hemisphere maximum number of eddies occurs during October (Figure 6e, g). Meanwhile, the seasonality of the eddy amplitude ($\langle |c\text{Eddy}_{amp}| \rangle$) peaks in August and January for the Northern and Southern Hemispheres respectively (Figure 6b, d, f, and h). As expected, the seasonality of $\langle |c\text{Eddy}_{amp}| \rangle$, equivalent to the intensity of the coherent eddies, is consistent with the seasonal cycle of $\langle \text{CEKE} \rangle$.

A key feature of Figure 6 is a distinct lag of ~ 3 months between the winds and eddy count, while the eddy amplitude maximum occurs ~ 6 months after the seasonal maxima in winds. We suggest that the eddy number increases earlier in the year and, through eddy-eddy interactions (merging of coherent eddies), the amplitude of the coherent eddy increases ~ 3 months after. This seasonal lag and summer maxima is consistent with pre-

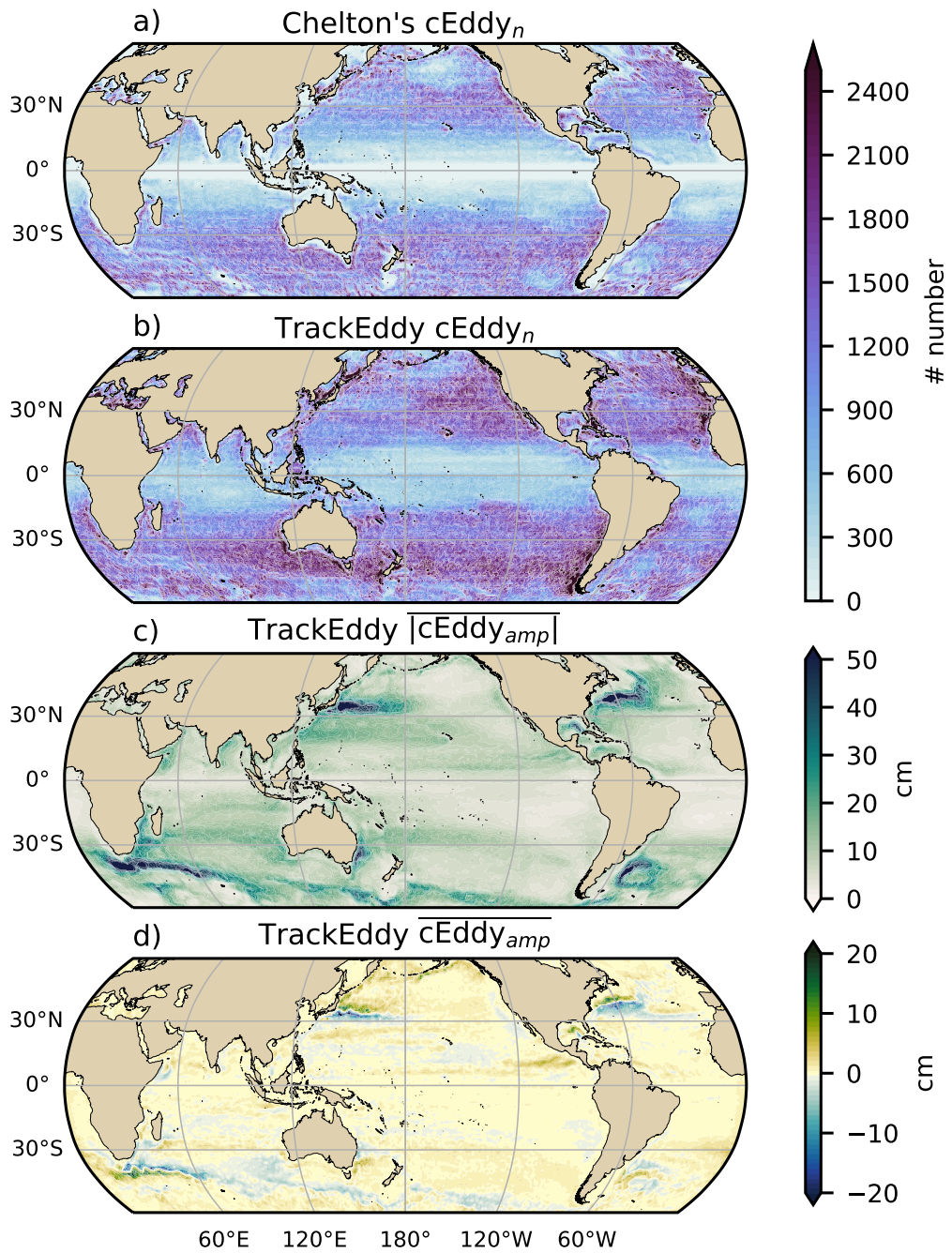
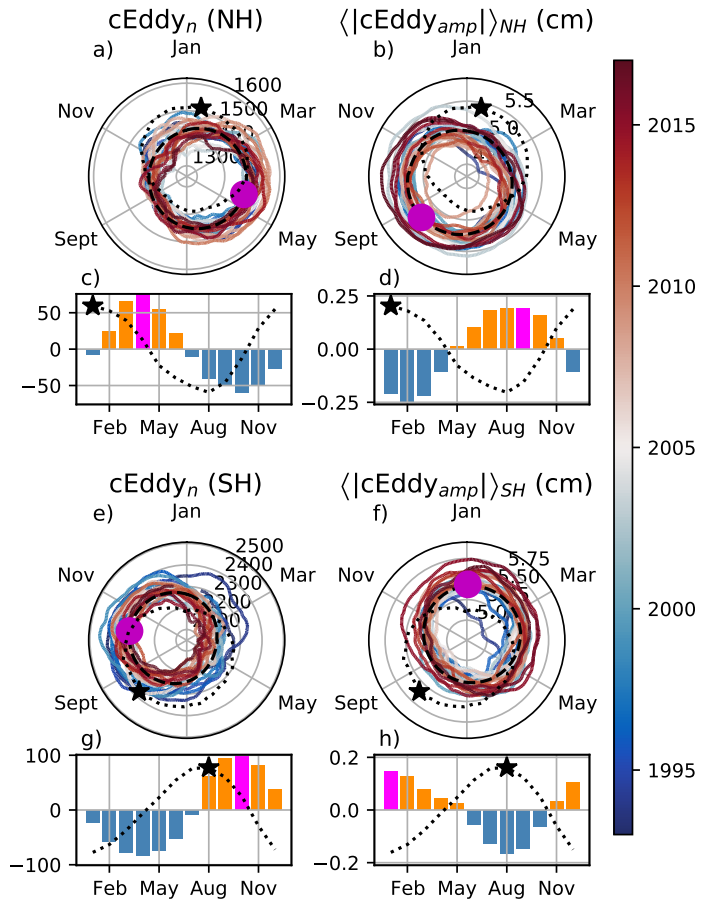


Figure 5. Averaged coherent eddy statistics. a) Climatology of the number of coherent eddies ($cEddy_n$) identified by Chelton et al. (2007); b) Climatology of the number of coherent eddies ($cEddy_n$) identified by Martínez-Moreno et al. (2019); c) Climatology of the mean absolute coherent eddy amplitude ($cEddy_{amp}$). d) Climatology of the mean coherent eddy amplitude ($cEddy_{amp}$).

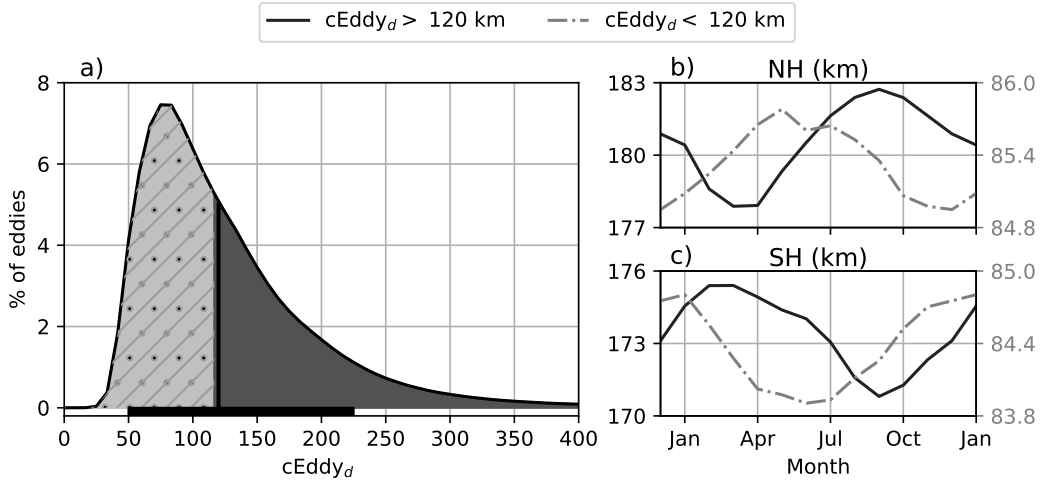
314 vious studies which suggest that a time-lag of the inverse cascade (Sasaki et al., 2014;
 315 Qiu et al., 2014) is responsible for the EKE seasonal cycle, where winter has the high-
 316 est energy at the smallest scales (non-resolvable with satellite observations), spring and
 317 autumn have the highest and lowest energy at scales of 50–100 km, and summertime has
 318 the highest energy at the largest scales (> 100 km; Uchida et al., 2017). Thus, the max-
 319 imum of $\langle \text{EKE} \rangle$, $\langle \text{CEKE} \rangle$, and $\langle |c\text{Eddy}_{amp}| \rangle$ located during summertime suggests that
 320 the seasonality of eddies and coherent eddies could be dominated by scales larger than
 321 100 km.

322 This result can be further explored by looking at the seasonal evolution of the eddy
 323 diameter ($c\text{Eddy}_d$). Note that 90% of identified coherent eddies have diameters between
 324 50 to 220 km (Figure 7a). We partition eddies into large-scale coherent eddies (diam-
 325 eter > 120 km) and small-scale coherent eddies (diameter < 120 km; Figure 7a). In the
 326 Northern Hemisphere, small-scale eddies have a seasonal peak in diameter during May,
 327 while large-scale eddies have the greatest diameter in September (Figure 7b). Meanwhile,
 328 in the Southern Hemisphere, the small-scale coherent eddies exhibit maximum diame-
 329 ter in December, while the diameter of large-scale coherent eddies peaks in February (Fig-
 330 ure 7 c). This result suggests that wind driven baroclinic instabilities generate small co-
 331 herent eddies early in the season, which then merge and grow to become larger in diam-
 332 eter and amplitude, and thus, more energetic. This process is likely associated with the
 333 inverse energy cascade, and suggests that this mechanism not only drives EKE season-
 334 ality, but also may be responsible for the seasonal cycle of coherent eddies.

350 Long-term changes can be observed in Figure 6a,b, e, and f where growing/shrinking
 351 concentric circles over time denote an increase/decrease trend of the field. This trend
 352 is particularly evident in the Southern Hemisphere, where the number of eddies has de-
 353 creased, while the eddy amplitude has increased. This result is consistent with the ob-
 354 served trends in EKE and mesoscale EKE in the Southern Ocean (Hogg et al., 2015; Martínez-
 355 Moreno et al., 2019). The coherent eddy amplitude from positive coherent eddies and
 356 negative coherent eddies show similar seasonal cycles to the absolute eddy amplitude.
 357 The Northern Hemisphere decrease in absolute eddy amplitude is driven by a decrease
 358 of the amplitude of negative coherent eddies in the Northern Hemisphere. Meanwhile
 359 in the Southern Ocean, the increase in absolute eddy amplitude is corroborated by a strength-
 360 ening of both coherent eddy polarities since the early 90s.



335 **Figure 6.** Seasonality of the count of number of eddies ($c\text{Eddy}_n$) and the area-weighted polar-
 336 ity independent coherent eddy amplitude ($\langle |c\text{Eddy}_{amp}| \rangle$); Panels a and b show the time-series of
 337 the Northern Hemisphere, while panels e and f correspond to the Southern Hemisphere. Panels c
 338 and d show the seasonal cycle of the $c\text{Eddy}_n$ and $\langle |c\text{Eddy}_{amp}| \rangle_{NH}$ in the Northern Hemisphere,
 339 and panels g and h show the Southern Hemisphere $c\text{Eddy}_n$ and $\langle |c\text{Eddy}_{amp}| \rangle_{SH}$. Dashed lines
 340 correspond to the seasonal cycle of the fields and dotted lines show the seasonal cycle of the
 341 wind magnitude, smoothed over 120 days (moving average). The black and magenta markers
 342 (circle and bar) indicate the maximum of the seasonal cycle for the eddy property, and the wind
 343 magnitude, respectively. In the cyclic plots, line colors show the year from 1993-2019.

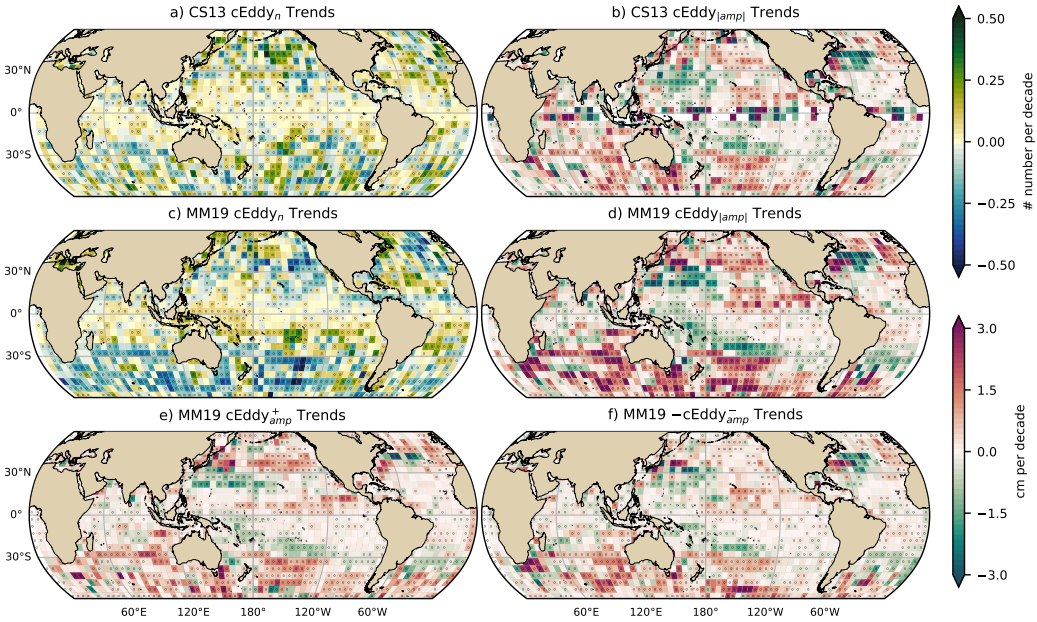


344 **Figure 7.** Distribution of the identified eddy diameter ($cEddy_d$; km) and hemispherical
 345 seasonality of the coherent eddy diameter. a) Distribution in percentage of identified eddy am-
 346 plitude, solid bar below distribution represents 90% of the identified eddies. Seasonal cycle of
 347 the eddy diameter for the b) Northern Hemisphere and c) Southern Hemisphere. Dark solid line
 348 and area corresponds to coherent eddies with diameters larger than 120 km, while light gray
 349 eddies with diameters smaller than 120 km.

361 5 Trends

362 The results presented in Figures 4 and 6 suggest a long-term readjustment of the
 363 coherent eddy field. The long-term trends of the number of coherent eddies, absolute co-
 364 herent eddy amplitude, and coherent eddy amplitude polarities are further explored in
 365 Figure 8 contrasting the MM19 and CS13 methods. MM19 and CS13 datasets show con-
 366 sistent spatial patterns in the trends and significance of the number of coherent eddies
 367 and the absolute coherent eddy amplitude. Several regions in the ocean, such as the South-
 368 ern Ocean, North Atlantic and North Pacific, show a decrease in the number of eddies.
 369 Those same regions also have a clear increase in the absolute coherent eddy amplitude.
 370 These trends are similar to those observed in mesoscale eddy kinetic energy (Martínez-
 371 Moreno et al., 2021) and provide additional evidence of a readjustment of the mesoscale
 372 eddy field over the last 3 decades.

373 The observed trends of $cEddy_{amp}$ in several oceanic regions have the same scale
 374 as sea level rise (~ 3 cm per decade). By analyzing the positive and negative coherent eddy
 375 amplitude, we filter out the observed trends that come from a net increase in sea level.



383 **Figure 8.** Trends of coherent eddy statistics. a) and b) Trends of the number of identified
 384 coherent eddies from satellite observations identified using the TrackEddy scheme of MM19,
 385 and those reported in CS13's dataset. c) and d) Trends of the absolute value of identified coher-
 386 ent eddy amplitude ($cEddy_{amp}$) from satellite observations identified using TrackEddy (after
 387 MM19), and those reported by CS13. e) and f) Trends of the eddy amplitude polarity using
 388 TrackEddy ($cEddy_{amp}^+$ and $cEddy_{amp}^-$). Gray stippling shows regions that are statistically signifi-
 389 cant above the 95% confidence level.

376 In fact, each coherent eddy polarity has intensified in the Southern Ocean and North East
 377 Pacific and Atlantic. In other words, the amplitude of each polarity has increased over
 378 time, and thus this strengthening is an intrinsic response of the coherent eddy field. Note
 379 that the negative coherent eddy amplitude dominates the global $|cEddy_{amp}|$ trends (Fig-
 380 ure 8e, f). However, different trend patterns can be observed in both positive and neg-
 381 ative coherent eddy amplitudes in the North Atlantic and North Pacific, where the neg-
 382 ative coherent eddy amplitude in the Western Boundary Currents appears to decrease.

390 6 Regional Climatology

391 For regions with relatively large proportions of CEKE located at WBCe and east-
 392 ern boundary currents, we investigate the seasonal and long-term variability of the co-
 393 herent eddy properties. The most energetic WBCe include the Gulf Stream, the Kuroshio

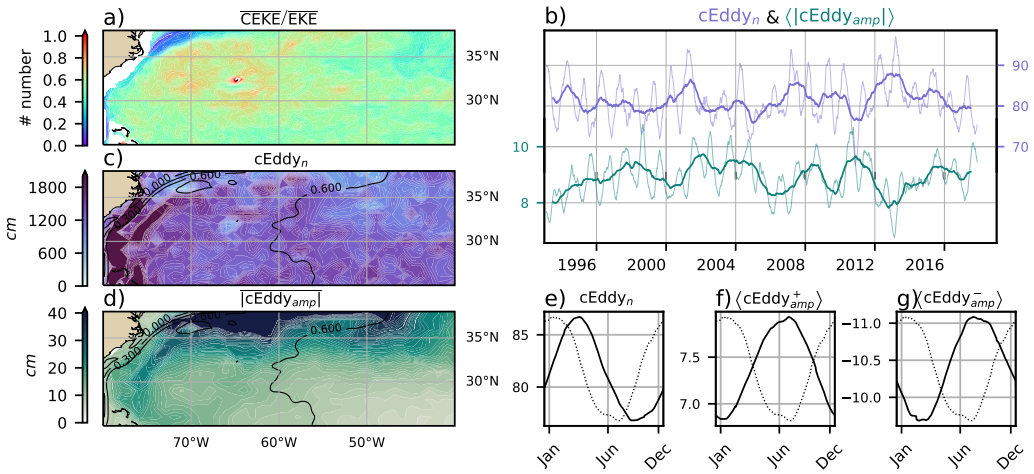
394 Current, and the Agulhas Current (Figures 9, 10, and 11). Coherent eddy generation in
 395 boundary current extensions occurs through baroclinic and barotropic instabilities of the
 396 mean current, thus all these regions share similar generation dynamics. In all these re-
 397 gions without exception; (i) CEKE contains 50-80% of the EKE in regions equatorward
 398 from the mean WBCe, (ii) the number of eddies is consistently small over the mean WBCe,
 399 and (iii) the eddy amplitude is larger over the mean WBCe.

400 In the Gulf Stream, the energy ratio between CEKE and EKE is \sim 56% (Figure 9).
 401 The highest energy ratio occurs in regions with numerous eddies, collocated with regions
 402 where the largest $|cEddy_{amp}|$ gradients occur. The time series of $cEddy_n$ and $\langle |cEddy_{amp}| \rangle$
 403 are anti-correlated (-0.52), and they display interannual and seasonal variability. Although
 404 Chaudhuri et al. (2009) observed that a positive phase of the North Atlantic Oscillation
 405 (NAO) exhibits higher EKE, due to an increase in baroclinic instability, thus suggest-
 406 ing more coherent eddies, we do not find a correlation between the $cEddy_n$ or the $\langle |cEddy_{amp}| \rangle$
 407 in the Gulf Stream and the NAO index. Similar to the signal observed in the hemispheric
 408 analysis, the eddy count seasonal cycle follows the wind maximum lagging by \sim 3 months,
 409 while the amplitude of the coherent eddies lags by \sim 6 months.

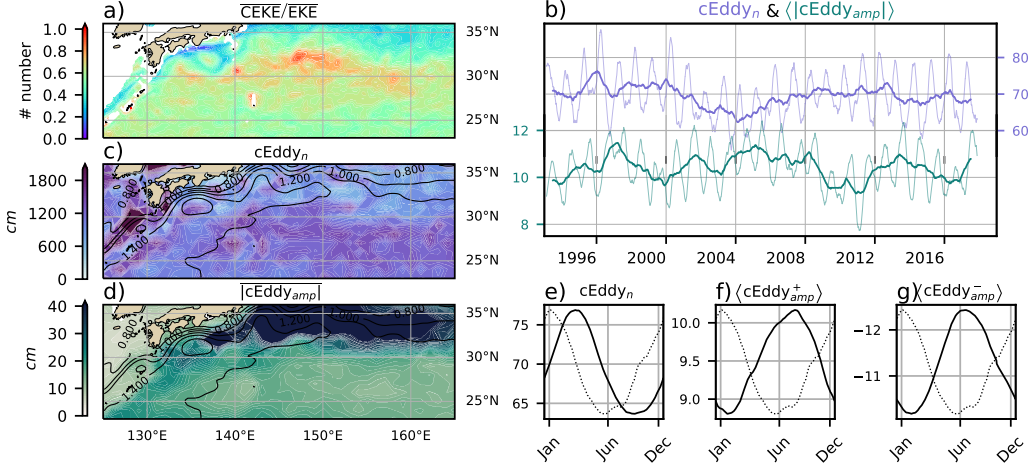
418 The variability of the $cEddy_n$ and $\langle |cEddy_{amp}| \rangle$ in the Kuroshio Current are weakly
 419 anti-correlated (-0.41; Figure 10). However, on average 56% of the energy in the region
 420 corresponds to CEKE. As observed in the Gulf Stream, there is an important seasonal
 421 cycle in the boundary extension, where the eddy count seasonal cycle occurs in March,
 422 lagging the wind maximum by \sim 3 months (January). Meanwhile, the amplitude of the
 423 coherent eddies lags the wind maximum by \sim 6 months (June).

430 In the Southern Hemisphere the strongest boundary current, the Agulhas Current,
 431 shows similar behavior to its counterparts in the Northern Hemisphere (Figure 11). On
 432 average, coherent eddies in the Agulhas Current contain \sim 56% of the energy, meanwhile
 433 the $cEddy_n$ seasonal peak occurs in August, while the $\langle |cEddy_{amp}| \rangle$ peak occurs in January-
 434 February. The seasonal lag between the winds, eddy count, and eddy amplitude in each
 435 of the WBCe is interpreted as being analogous to the lagged response of coherent eddy
 436 properties (Figure 6) due to eddy-eddy interactions, consistent with the inverse cascade
 437 of energy.

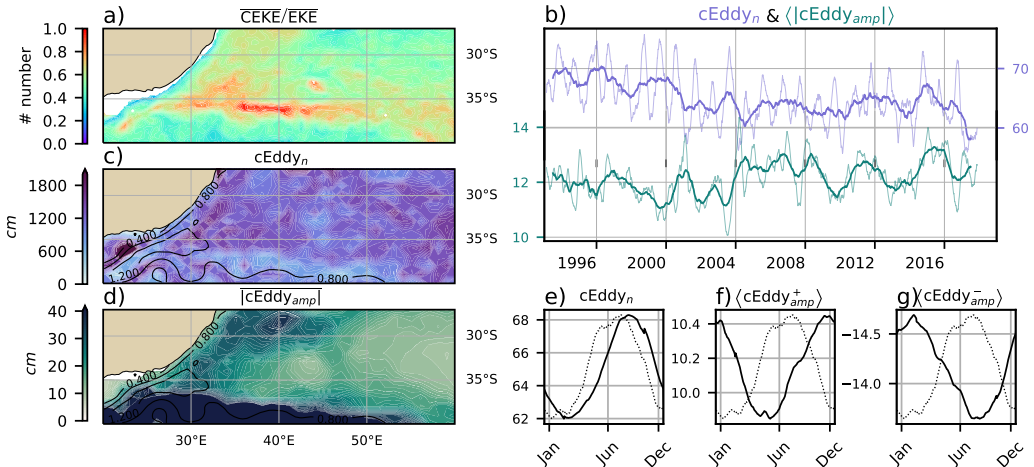
444 Coherent eddies dominate the EKE field in other regions such as the Leeuwin Cur-
 445 rent (Figure 12), where 65% of the energy is contained by coherent eddies. The Leeuwin



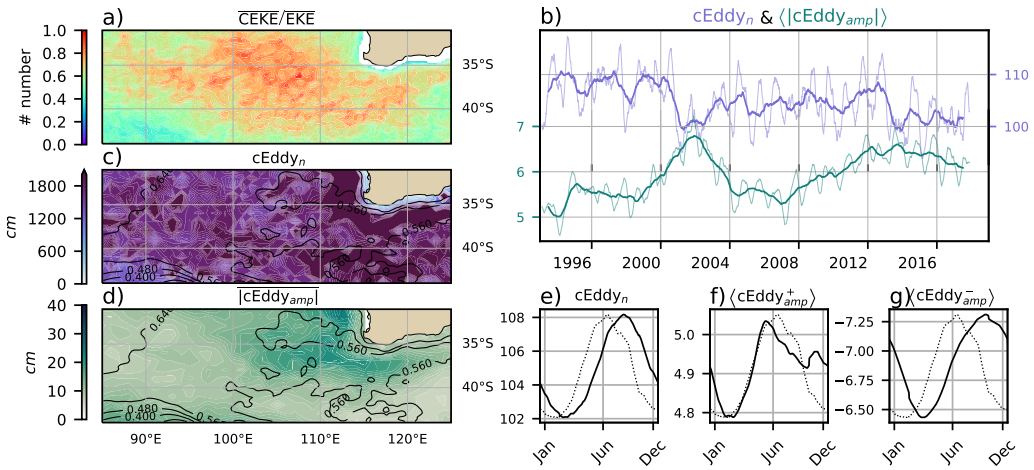
410 **Figure 9.** Climatology of the eddy field and coherent eddy field in the Gulf Stream. a) Ratio
 411 of mean coherent eddy kinetic energy (\overline{CEKE}) versus mean eddy kinetic energy (\overline{EKE}); b) Thick
 412 lines show the running average over 2 years and thin lines show the running average over 90 days
 413 of the coherent eddy number sum and the average coherent eddy amplitude; c) Map of the num-
 414 ber of eddies; d) Map of the average coherent eddy amplitude; e) Seasonal cycle of the number
 415 of eddies ($cEddy_n$); f) Seasonal cycle of the positive coherent eddy amplitude ($\langle cEddy_{amp}^+ \rangle$),
 416 and g) Seasonal cycle of the negative coherent eddy amplitude ($\langle cEddy_{amp}^- \rangle$). Contours in maps
 417 correspond to mean sea surface height (m).



424 **Figure 10.** As in Figure 9, climatology of the eddy field and coherent eddy field in the
 425 Kuroshio extension. a) Ratio of mean coherent eddy kinetic energy ($\overline{\text{CEKE}}$) versus mean eddy
 426 kinetic energy ($\overline{\text{EKE}}$); b) Time-series of the coherent eddy number and the average coherent eddy
 427 amplitude; c) Map of the number of eddies; d) Map of the average coherent eddy amplitude;
 428 Seasonal cycle of the e) number of eddies; f) positive coherent eddy amplitude, and g) negative
 429 coherent eddy amplitude.



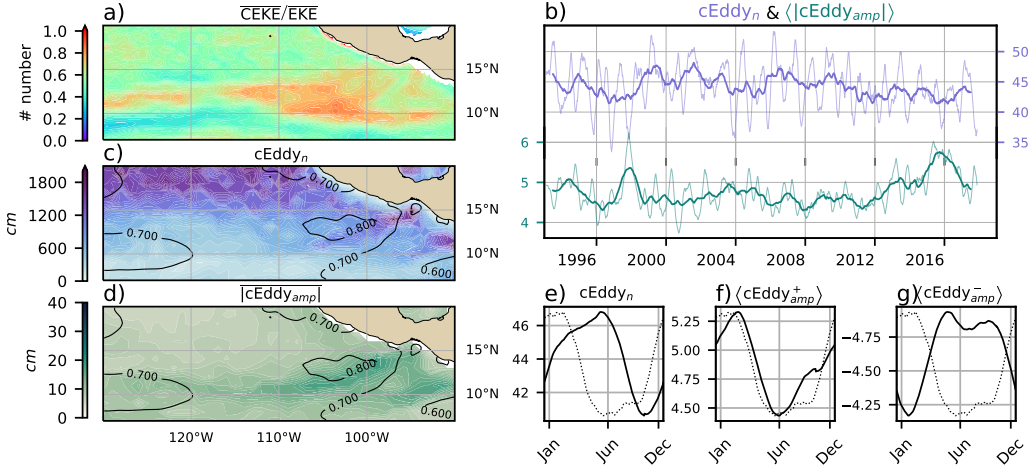
438 **Figure 11.** As in Figure 9, Climatology of the eddy field and coherent eddy field in the Ag-
 439 ulhas Current. a) Ratio of mean coherent eddy kinetic energy ($\overline{\text{CEKE}}$) versus mean eddy kinetic
 440 energy ($\overline{\text{EKE}}$); b) Time-series of the coherent eddy number and the average coherent eddy ampli-
 tude; c) Map of the number of eddies; d) Map of the average coherent eddy amplitude; Seasonal
 441 cycle of the e) number of eddies; f) positive coherent eddy amplitude, and g) negative coherent
 442 eddy amplitude.



454 **Figure 12.** As in Figure 9, climatology of the eddy field and coherent eddy field in the
 455 Leeuwin Current. a) Ratio of mean coherent eddy kinetic energy ($\overline{\text{CEKE}}$) versus mean eddy
 456 kinetic energy ($\overline{\text{EKE}}$); b) Time-series of the coherent eddy number and the average coherent eddy
 457 amplitude; c) Map of the number of eddies; d) Map of the average coherent eddy amplitude;
 458 Seasonal cycle of the e) number of eddies; f) positive coherent eddy amplitude, and g) negative
 459 coherent eddy amplitude.

446 region is not characterized by having a large EKE, however, a considerable abundance
 447 of eddies and large eddy amplitudes are observed in the region. The time-series reveal
 448 a significant increase in the $\langle |c\text{Eddy}_{amp}| \rangle$, while the $c\text{Eddy}_n$ has decreased over the last
 449 3 decades. The seasonal cycle shows that the $c\text{Eddy}_n$ peak occurs in August, 3 months
 450 after the maximum winds (June). Meanwhile, the $\langle c\text{Eddy}_{amp}^+ \rangle$ responds in synchrony
 451 to the winds, and the $\langle c\text{Eddy}_{amp}^- \rangle$ is in phase with the seasonal cycle of the eddy num-
 452 ber ($c\text{Eddy}_n$). Hence, this region contrast the behavior of WBCe, and showcases the spa-
 453 tial variability of the seasonal cycle of coherent eddies.

460 Another region with important contributions to the coherent eddy field is the East
 461 Tropical Pacific (Tehuantepec region; Figure 13), where coherent eddies contain $\sim 58\%$
 462 of the energy. In fact, coherent eddy generation in this region is modulated by winds and
 463 coastally trapped waves which produce a strong horizontal and vertical shear (baroclinic
 464 and barotropic instabilities; Zamudio et al., 2006). Furthermore, the equatorial gener-
 465 ated waves propagating along the coast have an important interannual variability ob-
 466 servable in the $\langle |c\text{Eddy}_{amp}| \rangle$ time-series, where El Niño events are notable during 1997



473 **Figure 13.** As in Figure 9, climatology of the eddy field and coherent eddy field in the East
 474 Tropical Pacific. a) Ratio of mean coherent eddy kinetic energy ($\overline{\text{CEKE}}$) versus mean eddy ki-
 475 netic energy ($\overline{\text{EKE}}$); b) Time-series of the coherent eddy number and the average coherent eddy
 476 amplitude; c) Map of the number of eddies; d) Map of the average coherent eddy amplitude;
 477 Seasonal cycle of the e) number of eddies; f) positive coherent eddy amplitude, and g) negative
 478 coherent eddy amplitude.

467 and 2015 (Figure 13b). The seasonal cycle of $c\text{Eddy}_n$, $\langle c\text{Eddy}_{amp}^+ \rangle$, and $\langle c\text{Eddy}_{amp}^- \rangle$ sup-
 468 port the idea of a coherent eddy response to two different coherent eddy generation mech-
 469 anisms; the number of eddies lags by ~ 3 months from the winds, while the $\langle c\text{Eddy}_{amp}^+ \rangle$
 470 is in phase with the winds and the time of maximum trapped wave activity (winter; Za-
 471 mudio et al., 2006), while the $\langle c\text{Eddy}_{amp}^- \rangle$ could be a consequence of eddy-eddy inter-
 472 actions.

479 7 Discussion and Conclusions

480 We have investigated the contribution of coherent eddies to the total kinetic en-
 481 ergy field using available satellite observations. We found that around half of the EKE
 482 is explained by coherent eddies. This half is concentrated in eddy-rich regions where a
 483 recent multi-decadal intensification of the eddy field has been observed (Martínez-Moreno
 484 et al., 2021). The energy contained by eddies is larger than the previous estimate of 40%
 485 by Chelton et al. (2011). Although there are differences in the identification criteria of
 486 both eddy identification methods, the main cause of the difference is likely to be the lifes-

pan and amplitude filters. These filters are widely used to track individual eddies in space and time, however, interactions between eddies in energetic regions may obscure the abundance and influence of short-lived coherent eddies. Filters are not used in this study, and indeed a lack of filters could facilitate an over-estimation of the energy contained by coherent eddies, when mis-identifying or mis-fitting a coherent eddy. In hindsight, current generation of climate models have just started to resolve mesoscale dynamics, thus, the presented estimate of energy in coherent eddies from satellite observations could be used as a benchmark and quantify the energy contained by mesoscale and more specifically coherent eddies in future climate models.

It should also be noted that regions with first baroclinic Rossby radius of deformation smaller than 10km cannot be resolved by satellite observations. Thus, the energy contained by coherent eddies around latitudes of 60° and those near the shore are missed from this estimate, and their role in the seasonal cycle and local dynamics remains unknown. New satellite altimeter missions (e.g. Surface Water and Ocean Topography; SWOT) may allow estimates of the energy contained by mesoscale coherent eddies outside the tropical region and the continental slope.

Hemisphere-wide variability indicates a strong seasonal cycle of the EKE, CEKE, and eddy properties. The seasonal cycle of the CEKE in each hemisphere occurs as a consequence of numerous small coherent eddies interacting with each other (eddy-eddy interactions) and resulting in stronger, larger and more energetic (but fewer) coherent eddies during summer, after a few months of the yearly coherent eddy number maxima. This result reveals eddy-eddy interactions and thus the transfer of energy from smaller coherent eddies to larger coherent eddies could explain the observed seasonal cycle of CEKE and coherent eddies properties.

Coherent eddy properties reveal a non-uniform long-term readjustment of the mesoscale eddy field. Overall, the eddy number has decreased globally at a significant rate of ~ 35 eddies per decade from ~ 4000 eddies identified globally on average each day. Despite the small changes in the eddy numbers, large proportions of the ocean show a major strengthening of the mesoscale coherent eddy amplitude at rates greater than ~ 1 cm per decade. This strengthening of the coherent eddy amplitude is attributed to an intensification of each coherent eddy polarity, rather than a readjustment of the coherent eddy field to sea level rise. In other words, the coherent eddy amplitude intensification is occurring in both

519 coherent eddy polarities and explains a proportion of the previously observed readjust-
 520 ments in the eddy field to long-term changes in the ocean forcing (Hu et al., 2020; Wun-
 521 sch, 2020; Martínez-Moreno et al., 2021). This long-term readjustment reveals an inten-
 522 sification of the coherent eddy field, possibly due to long-term readjustments in the ocean
 523 baroclinic and barotropic instabilities, as well as the strength of the winds.

524 The reconstruction of the coherent eddies and their statistics has revealed regions
 525 with important coherent eddy contributions and a distinct seasonal evolution of the co-
 526 herent eddies. Western boundary current extensions (WBCe) generate eddies through
 527 the instability of the main currents and the seasonal cycle of coherent eddies, CEKE, and
 528 thus EKE could be associated with an inverse energy cascade observable through lagged
 529 seasonal cycles in the coherent eddy statistics. In addition, the amplitude of the seasonal
 530 cycle in WBCe is two times larger than any other region, thus the seasonality of the co-
 531 herent eddies in WBCe dominates the hemispheric seasonal cycle. Furthermore, the sea-
 532 sonal lag of the inverse energy cascade is coupled with the presence of fronts (Qiu et al.,
 533 2014), such is the case for WBCe, and our results are consistent with the notion of baro-
 534 clinic instability generating eddies and, via eddy-eddy interactions, a lagged inverse en-
 535 ergy cascade.

536 The use of satellite observations in this study limits our ability to quantify the im-
 537 portance of the inverse energy cascade seasonality in the control of the coherent eddy
 538 seasonal cycle. As mentioned above, there is robust evidence of an increase in eddy-eddy
 539 interactions, however we cannot discard important contributions from other processes
 540 such as the seasonal cycle of forcing, stratification, and instabilities, which are crucial
 541 in the generation of coherent eddies. Although this study can provide a descriptive re-
 542 sponse of the coherent eddy field, further work is needed to asses the role of eddy-
 543 eddy interactions in our changing climate, ocean dynamics, and biogeochemical process.
 544 Furthermore, the SWOT mission could allow us to advance our understanding of eddy-
 545 eddy interactions and the seasonal cycle of scales smaller than mesoscale, which may pro-
 546 vide further evidence of the inverse energy cascade driving the coherent eddy seasonal-
 547 ity.

548 Acknowledgments

549 The Chelton & Schlax (2013) dataset was produced by SSALTO/DUACS and distributed
 550 by AVISO+ (<https://www.aviso.altimetry.fr/>) with support from CNES, developed

and validated in collaboration with E.Mason at IMEDEA. Global coherent eddy reconstruction, coherent and non-coherent eddy kinetic energy datasets, in addition to grid-ded coherent eddy tracking datasets are publicly available at (<https://doi.org/10.5281/zenodo.4646429>). All analyses and figures in this manuscript are reproducible via Jupyter notebooks and instructions can be found in the Github repository `CEKE_climatology` (https://github.com/josuemtzmo/CEKE_climatology). Trends used the Python Package `xarrayMannKendall` (<https://doi.org/10.5281/zenodo.4458776>). J.M.-M. was supported by the Consejo Nacional de Ciencia y Tecnología (CONACYT), Mexico funding. M.H.E. is supported by the Centre for Southern Hemisphere Oceans Research (CSHOR), a joint research centre between Qingdao National Laboratory for Marine Science and Technology (QNLM), Commonwealth Scientific and Industrial Research Organisation (CSIRO), University of New South Wales (UNSW), and the University of Tasmania (UTAS). Analyses were undertaken on the National Computational Infrastructure in Canberra, Australia, which is supported by the Australian Commonwealth Government.

References

- Arbic, B. K., Polzin, K. L., Scott, R. B., Richman, J. G., & Shriver, J. F. (2013). On Eddy Viscosity, Energy Cascades, and the Horizontal Resolution of Gridded Satellite Altimeter Products*. *Journal of Physical Oceanography*, *43*(2), 283–300. doi: [10.1175/jpo-d-11-0240.1](https://doi.org/10.1175/jpo-d-11-0240.1)
- Ashkezari, M. D., Hill, C. N., Follett, C. N., Forget, G., & Follows, M. J. (2016). Oceanic eddy detection and lifetime forecast using machine learning methods. *Geophysical Research Letters*, *43*(23). doi: [10.1002/2016gl071269](https://doi.org/10.1002/2016gl071269)
- Beron-Vera, F. J., Wang, Y., Olascoaga, M. J., Goni, G. J., & Haller, G. (2013). Objective Detection of Oceanic Eddies and the Agulhas Leakage. *Journal of Physical Oceanography*, *43*(7), 1426–1438. doi: [10.1175/JPO-D-12-0171.1](https://doi.org/10.1175/JPO-D-12-0171.1)
- Bouali, M., Sato, O. T., & Polito, P. S. (2017). Temporal trends in sea surface temperature gradients in the South Atlantic Ocean. *Remote Sensing of Environment*, *194*, 100–114. doi: [10.1016/j.rse.2017.03.008](https://doi.org/10.1016/j.rse.2017.03.008)
- Callies, J., Flierl, G., Ferrari, R., & Fox-Kemper, B. (2015). The role of mixed-layer instabilities in submesoscale turbulence. *Journal of Fluid Mechanics*, *788*, 5–41. doi: [10.1017/jfm.2015.700](https://doi.org/10.1017/jfm.2015.700)
- Cane, M. A., Clement, A. C., Kaplan, A., Kushnir, Y., Pozdnyakov, D., Seager, R.,

- 583 ... Murtugudde, R. (1997). Twentieth-Century Sea Surface Temperature Trends.
584 *Science*, 275(5302), 957–960. doi: 10.1126/science.275.5302.957
- 585 Chaudhuri, A. H., Gangopadhyay, A., & Bisagni, J. J. (2009). Interannual variabil-
586 ity of Gulf Stream warm-core rings in response to the North Atlantic Oscillation.
587 *Continental Shelf Research*, 29(7), 856–869. doi: 10.1016/j.csr.2009.01.008
- 588 Chelton, D. B., A. d. R., Schlax, M. G., Naggar, K., & Siwetz, N. (1998). Geo-
589 graphical variability of the first baroclinic Rossby radius of deformation. *Journal*
590 *of Physical Oceanography*, 28(3), 433-460. doi: 10.1175/1520-0485(1998)028<0433:
591 GVOTFB>2.0.CO;2
- 592 Chelton, D. B., Gaube, P., Schlax, M. G., Early, J. J., & Samelson, R. M. (2011).
593 The influence of nonlinear mesoscale eddies on near-surface oceanic chlorophyll.
594 *Science*, 334(6054), 328-32. doi: 10.1126/science.1208897
- 595 Chelton, D. B., & Schlax, M. G. (2013). *Mesoscale eddies in altimeter observations*
596 *of ssh.*
- 597 Chelton, D. B., Schlax, M. G., Samelson, R. M., & de Szoeke, R. A. (2007). Global
598 observations of large oceanic eddies. *Geophysical Research Letters*, 34(15),
599 L15606. doi: 10.1029/2007GL030812
- 600 CMEMS. (2017). The Ssalto/Duacs altimeter products were produced and dis-
601 tributed by the Copernicus Marine and Environment Monitoring Service. *Aviso*
602 *Dataset*. Retrieved from <https://www.aviso.altimetry.fr/>
- 603 Cui, W., Wang, W., Zhang, J., & Yang, J. (2020). Identification and census statis-
604 tics of multicore eddies based on sea surface height data in global oceans. *Acta*
605 *Oceanologica Sinica*, 39(1), 41–51. doi: 10.1007/s13131-019-1519-y
- 606 Faghmous, J. H., Frenger, I., Yao, Y., Warmka, R., Lindell, A., & Kumar, V. (2015,
607 6). A daily global mesoscale ocean eddy dataset from satellite altimetry. *Scientific*
608 *Data*, 2, 150028 EP -. doi: 10.1038/sdata.2015.28
- 609 Ferrari, R., & Wunsch, C. (2009). Ocean Circulation Kinetic Energy: Reservoirs,
610 Sources, and Sinks. *Annual Review of Fluid Mechanics*, 41(1), 253–282. doi: 10
611 .1146/annurev.fluid.40.111406.102139
- 612 Frenger, I., Gruber, N., Knutti, R., & Münnich, M. (2013). Imprint of Southern
613 Ocean eddies on winds, clouds and rainfall. *Nature Geoscience*, 6(8), 608 EP -.
614 doi: 10.1038/ngeo1863
- 615 Frenger, I., Münnich, M., Gruber, N., & Knutti, R. (2015). Southern Ocean eddy

- phenomenology. *Journal of Geophysical Research: Oceans*, 120(11), 7413-7449.
doi: 10.1002/2015JC011047
- Fu, L., Chelton, D., Le Traon, P., & Oceanography, M. R. (2010). Eddy dynamics from satellite altimetry. *Oceanography*, 23(4), 14-25. doi: 10.2307/24860859
- Gill, A., Green, J., & Simmons, A. (1974). Energy partition in the large-scale ocean circulation and the production of mid-ocean eddies. *Deep Sea Res Oceanogr Abstr*, 21(7), 499-528. doi: 10.1016/0011-7471(74)90010-2
- Hogg, A. M., & Blundell, J. R. (2006). Interdecadal variability of the southern ocean. *Journal of Physical Oceanography*, 36(8), 1626-1645. doi: 10.1175/JPO2934.1
- Hogg, A. M., Meredith, M. P., Chambers, D. P., Abrahamsen, E. P., Hughes, C. W., & Morrison, A. K. (2015). Recent trends in the Southern Ocean eddy field. *Journal of Geophysical Research: Oceans*, 120(1), 257-267. doi: 10.1002/2014JC010470
- Hu, S., Sprintall, J., Guan, C., McPhaden, M. J., Wang, F., Hu, D., & Cai, W. (2020, 2). Deep-reaching acceleration of global mean ocean circulation over the past two decades. *Science Advances*, 6(6), eaax7727. doi: 10.1126/sciadv.aax7727
- Japan Meteorological Agency, Japan. (2013). *Jra-55: Japanese 55-year reanalysis, daily 3-hourly and 6-hourly data*. Boulder CO: Research Data Archive at the National Center for Atmospheric Research, Computational and Information Systems Laboratory. Retrieved from <https://doi.org/10.5065/D6HH6H41>
- Kang, D., & Curchitser, E. N. (2013). Gulf stream eddy characteristics in a high-resolution ocean model. *Journal of Geophysical Research: Oceans*, 118(9), 4474-4487. Retrieved from <https://agupubs.onlinelibrary.wiley.com/doi/abs/10.1002/jgrc.20318> doi: <https://doi.org/10.1002/jgrc.20318>
- Kang, D., & Curchitser, E. N. (2017). On the Evaluation of Seasonal Variability of the Ocean Kinetic Energy. *Geophysical Research Letters*, 47, 1675-1583. doi: 10.1175/JPO-D-17-0063.1
- Li, G., Cheng, L., Zhu, J., Trenberth, K. E., Mann, M. E., & Abraham, J. P. (2020). Increasing ocean stratification over the past half-century. *Nature Climate Change*, 1-8. doi: 10.1038/s41558-020-00918-2
- Martínez-Moreno, J., Hogg, A. M., England, M., Constantinou, N. C., Kiss, A. E.,

- 649 & Morrison, A. K. (2021). Global changes in oceanic mesoscale currents over the
650 satellite altimetry record. *Journal of Advances in Modeling Earth Systems*, 0(ja).
651 doi: 10.1029/2019MS001769
- 652 Martínez-Moreno, J., Hogg, A. M., Kiss, A. E., Constantinou, N. C., & Morrison,
653 A. K. (2019). Kinetic energy of eddy-like features from sea surface altimeter-
654 try. *Journal of Advances in Modeling Earth Systems*, 11(10), 3090-3105. doi:
655 10.1029/2019MS001769
- 656 Patel, R. S., Llort, J., Strutton, P. G., Phillips, H. E., Moreau, S., Pardo, P. C.,
657 & Lenton, A. (2020). The Biogeochemical Structure of Southern Ocean
658 Mesoscale Eddies. *Journal of Geophysical Research: Oceans*, 125(8). doi:
659 10.1029/2020jc016115
- 660 Pilo, G. S., Mata, M. M., & Azevedo, J. L. L. (2015). Eddy surface properties and
661 propagation at Southern Hemisphere western boundary current systems. *Ocean
662 Science*, 11(4), 629–641. doi: 10.5194/os-11-629-2015
- 663 Qiu, B. (1999). Seasonal Eddy Field Modulation of the North Pacific Subtropical
664 Countercurrent: TOPEX/Poseidon Observations and Theory. *Journal of Physical
665 Oceanography*, 29(10), 2471–2486. doi: 10.1175/1520-0485(1999)029<2471:sefmot>2
666 .0.co;2
- 667 Qiu, B., & Chen, S. (2004). Seasonal Modulations in the Eddy Field of the South
668 Pacific Ocean. *Journal of Physical Oceanography*, 34(7), 1515–1527. doi: 10.1175/
669 1520-0485(2004)034<1515:smitef>2.0.co;2
- 670 Qiu, B., Chen, S., Klein, P., Sasaki, H., & Sasai, Y. (2014). Seasonal Mesoscale
671 and Submesoscale Eddy Variability along the North Pacific Subtropical Coun-
672 tercurrent. *Journal of Physical Oceanography*, 44(12), 3079–3098. doi:
673 10.1175/JPO-D-14-0071.1
- 674 Ruela, R., Sousa, M. C., deCastro, M., & Dias, J. M. (2020). Global and regional
675 evolution of sea surface temperature under climate change. *Global and Planetary
676 Change*, 190, 103190. doi: 10.1016/j.gloplacha.2020.103190
- 677 Sasaki, H., Klein, P., Qiu, B., & Sasai, Y. (2014). Impact of oceanic-scale inter-
678 actions on the seasonal modulation of ocean dynamics by the atmosphere. *Nature
679 Communications*, 5(1), 5636. doi: 10.1038/ncomms6636
- 680 Schubert, R., Schwarzkopf, F. U., Baschek, B., & Biastoch, A. (2019). Submesoscale
681 Impacts on Mesoscale Agulhas Dynamics. *Journal of Advances in Modeling Earth*

- 682 *Systems*, 11(8), 2745–2767. doi: 10.1029/2019ms001724
- 683 Siegel, D., Peterson, P., DJ, M., Maritorena, S., & Nelson, N. (2011). Bio-optical
684 footprints created by mesoscale eddies in the Sargasso Sea. *Geophysical Research
685 Letters*, 38(13), n/a-n/a. doi: 10.1029/2011GL047660
- 686 Uchida, T., Abernathey, R., & Smith, S. (2017). Seasonality of eddy kinetic energy
687 in an eddy permitting global climate model. *Ocean Modelling*, 118, 41-58. doi: 10
688 .1016/j.ocemod.2017.08.006
- 689 Wunsch, C. (2020). Is The Ocean Speeding Up? Ocean Surface Energy Trends.
690 *Journal of Physical Oceanography*, 50(11), 1–45. doi: 10.1175/jpo-d-20-0082.1
- 691 Wunsch, C., & Ferrari, R. (2004). Vertical mixing, energy, and the general circula-
692 tion of the oceans. *Annual Review of Fluid Mechanics*, 36(1), 281–314. doi: 10
693 .1146/annurev.fluid.36.050802.122121
- 694 Wyrtki, K., Magaard, L., & Hager, J. (1976). Eddy energy in the oceans. *Journal of
695 Geophysical Research*, 81(15), 2641-2646. doi: 10.1029/JC081i015p02641
- 696 Yue, S., & Wang, C. (2004). The Mann-Kendall Test Modified by Effective Sample
697 Size to Detect Trend in Serially Correlated Hydrological Series. *Water Resources
698 Management*, 18(3), 201–218. doi: 10.1023/b:warm.0000043140.61082.60
- 699 Zamudio, L., Hurlburt, H. E., Metzger, E. J., Morey, S. L., O'Brien, J. J., Tilburg,
700 C., & Zavala-Hidalgo, J. (2006). Interannual variability of Tehuantepec ed-
701 dies. *Journal of Geophysical Research: Oceans (1978–2012)*, 111(C5). doi:
702 10.1029/2005JC003182